Tellus
SINCE 1948

Impacts of Model Resolution on Ocean Internal Variability in the Northern North Atlantic Analyzed within the Framework of AR(1)-Process

RESEARCH ARTICLES

LIN LIN
JIN-SONG VON STORCH
HANS VON STORCH

*Author affiliations can be found in the back matter of this article

STOCKHOLM UNIVERSITY PRESS

ABSTRACT

Higher-resolution models explicitly resolve smaller-scale processes, thereby tending to enhance internal variability. While this perspective is well recognized and has been extensively investigated, a system-oriented perspective has received less attention and may offer complementary insight into the nature of internal variability. The system-oriented perspective refers to analyzing the climate system as a whole in terms of statistics. We explain the impacts of model grid resolution on the internal variability in the northern North Atlantic, focusing on two factors—memory and fluctuating forcing—within the framework of a first-order autoregressive (AR(1)) process, an exact form of the integral fluctuation–dissipation relation but associated with a single integration time interval. The ICON-ocean model is applied at grid resolutions of 20, 10, and 5 km, under identical daily climatological atmospheric forcing. Being captured by the AR(1)-framework, the total variance can be studied in terms of the two factors of the AR(1)-process: memory and fluctuating forcing. We find that the larger the variance of fluctuating forcing, the shorter the memory. Due to this general relationship, increasing horizontal resolution, allowing more variability to be resolved, leads to a strengthening of fluctuating forcing and a decrease in memory at the grid-point level. At both the grid-point level and across different spatial scales, increasing grid resolution has a stronger effect on the fluctuating forcing than on the memory, causing the total variance of internal variability to increase with increasing resolution.

CORRESPONDING AUTHOR:
Lin Lin
Max Planck Institute for Meteorology, Hamburg, Germany
lin.lin@mpimet.mpg.de

KEYWORDS:
statistical analysis; high-resolution ocean modeling; internal variability

TO CITE THIS ARTICLE:
Lin, L., von Storch, J.-S., & von Storch, H. (2026). Impacts of Model Resolution on Ocean Internal Variability in the Northern North Atlantic Analyzed within the Framework of AR(1)-Process. *Tellus, 79*(1), 232–248. https://doi.org/10.16993/tellus.4138

1. INTRODUCTION

1.1 RESEARCH GAP AND RESEARCH QUESTIONS

Numerical model grid resolution can strongly affect climate simulations. Most previous studies investigate the grid resolution effect from the process perspective, thereby focusing on how grid resolution impacts the model performance in simulating various phenomena and physical processes. It has been shown that increasing grid resolution improves the simulation of extreme weather, including tropical cyclones and heavy precipitation (Bador et al., 2020; Roberts et al., 2020), and the fidelity of simulated Atlantic Meridional Overturning Circulation and interannual sea-level variability in eddy-active regions, thereby reducing biases in mean temperature, salinity, mixed layer depth, and ocean circulations (Grégorio et al., 2015; Penduff et al., 2011; Wang et al., 2025). Most significantly, increasing horizontal resolution of ocean models improves the representation of oceanic fronts, mesoscale eddies, and topographically influenced processes (Bilgen & Kirtman, 2020; Hirschi et al., 2013; Wang et al., 2024) by explicitly resolving sharp frontal gradients and eddy–mean flow interactions, which are critical for accurate simulations of heat transport, current systems, and variability in regions such as the Southern Ocean and the Arctic (Bilgen & Kirtman, 2020; Wang et al., 2024).

Grid resolution effects can also be studied from the system perspective, thereby focusing on how resolution impacts the overall behaviors quantified by statistics. One of such statistics is the variance, a key quantity measuring the intensity of internal variability. Another is memory, often described by the autocorrelation at a particular lag. Memory is often linked to dissipation: the stronger the dissipation, the shorter the memory. Lin, H. von Storch, and Chen (2023) showed that memory plays an important role in determining the strength of internal variability, albeit addressing the role of tides rather than that of resolution for memory. In a recent study, Chen et al. (2025) showed that grid resolution impacts the memory of the Southern Annular Mode (SAM). Relative to observations, the SAM tends to be overly persistent—that is, it has an excessively long memory in CMIP6 simulations with a horizontal resolution of order 100 km. This bias is reduced in the EERIE simulations (https://eerie-project.eu) with a horizontal grid resolution of 9–25 km, which demonstrates that increasing grid resolution leads to a reduction in the memory of SAM (Chen et al., 2025).

Following the same system perspective, this paper examines how model grid resolution influences oceanic internal variability, focusing on its intensity and memory. This system perspective does not contradict process-based analyses. Rather, it complements them by considering the integrated effect of all interacting physical processes after the system has been evolved forward in time. As formalized below through the so-called integral forcing, the statistics of a given variable are influenced not only by processes acting directly on that variable but also by all other components that interact with it. In this sense, the system perspective provides a more integrated view of how grid resolution affects internal variability. Since the principle of the integrated effect is quite general, we expect that the grid resolution effect reported by Chen et al. (2025) for atmospheric models—namely, that increasing grid resolution reduces memory—should also be effective for the ocean, at least when increasing resolution generates increasingly stronger fluctuations. The goal of this paper is hence twofold. First, we want to check whether and to what extent this is indeed the case. Second, since the grid resolution effect has not been investigated through the lens of integral forcing, we aim to quantify how grid resolution changes the properties of integral forcing, thereby impacting the relation between memory and variance.

1.2 CONCEPTUAL FRAMEWORK

According to Hasselmann's stochastic climate model, a stationary climate results from a variance generation mechanism that involves fluctuating forcing arising from fast climate components and negative feedbacks related to dissipative processes (Hasselmann, 1976). While the fluctuating forcing constantly excites slow climate components, the negative feedbacks counteract the permanent stationary excitations, which results in stationary variations. While this concept is powerful, its direct application to concrete phenomena—such as internal oceanic variability to be studied in this paper—is not straightforward. The main problem is how to derive a stochastic description from the underlying deterministic equations. Generally, such a derivation relies on assumptions about the underlying dynamics—most crucially, the timescale-separation assumption.

In a series of recent studies (J.-S. von Storch, 2022, 2024, 2026), a concept that does not rely on any assumption about the dynamics has been proposed in several steps. We consider systems that evolve according to equations in the form

$$\frac{dx}{dt} = F(\mathrm{X}), \tag{1}$$

where F is a generally non-linear function of the full state vector X, and x is a component of X. The first step concerns the origin of randomness. Instead of introducing fluctuating forcing using scaling assumptions, randomness is identified as an inherent feature of a system in dynamical equilibrium (J.-S. von Storch, 2022). Here, 'dynamical equilibrium' refers to an equilibrium achieved by a forced-dissipative system under constant external forcing. 'Randomness' refers to the lack of serial correlations in the solution of the considered system for sufficiently large time lags. The emergence of such randomness gives rise to a spectrum that has a non-zero spectral value at frequency zero.

In the second step, the value of the spectrum of x at frequency zero is shown to be not determined by the differential forcing $F(\mathrm{X})$ of x, but by time integrals of $F(\mathrm{X})$, also referred to as the integral forcing G_τ of x (J.-S. von Storch, 2024). In a climate model, in which time is discretized using a step Δt, this forcing can be written as

$$G_{\tau,i} = \sum_{j=i}^{i+\tau-1} F_j \Delta t,\ \tau \in \mathbb{Z}_+ \tag{2}$$

where $\mathbb{Z}_+$ is the set of positive integers. The first subscript of $G_{\tau,i}$ indicates the duration over which the integration is carried out, and the second one the time at which the integration starts. Given the initial state x_i, $G_{\tau,i}$ determines the state of x τ time steps later:

$$x_{i+\tau} = x_i + G_{\tau,i} \tag{3}$$

Apart from a constant c_τ, which is related to the mean and will be dropped when considering anomalies, it is postulated that $G_{\tau,i}$ can always be decomposed into a dissipation of x, $d_\tau x$, and a fluctuating forcing $f_{\tau,i}$,

$$G_{\tau,i} = d_\tau x_i + f_{\tau,i},\ \tau \in \mathbb{Z}_+. \tag{4}$$

d_τ lies in the range (–2, 0) and is related to the auto-correlation function ρ_τ of x via

$$\rho_\tau = d_\tau + 1. \tag{5}$$

d_τ measures the strength of the total dissipation experienced by x within τ time steps. It arises not only from the direct damping of x included in Eq. (1) but also from the direct damping of all components of X that interact with x. As the latter is not included in Eq. (1), its effect becomes apparent only when integrating the whole system forward in time, after the interactions have taken place. This is also the reason why the total dissipation of x cannot be solely captured by its differential forcing F, but has to be described by its integral forcing G_τ.

The maximum total dissipation, which leads to the complete elimination of the initial state x_i in Eq.(3), is reached when $d_\tau = -1$, corresponding to $\rho_\tau = 0$. Once this happens for τ larger than a threshold value, randomness occurs. The auto-covariance function γ_τ becomes summable so that the spectrum $S(f)$ exists as the cosine Fourier transform of γ_τ:

$$S(f) = \sum_{\tau=-\infty}^{\infty} \gamma_\tau \cos(2\pi\tau f), \tag{6}$$

with a well-defined non-zero value at frequency zero, $S(0) = \Sigma_{\tau=-\infty}^{\infty} \gamma_\tau$. Thus, it is the total dissipation encoded in G_τ that causes the lack of serial correlation, which on the one hand makes the solution apparently random, and on the other hand produces the key feature of this randomness in the form of a well-defined $S(0) \neq 0$.

The expression of $G_{\tau,i}$ given in Eq. (4) is inspired by the classical fluctuation–dissipation theorem. This theorem essentially states that, for a system in dynamical equilibrium, anything that generates fluctuations must damp fluctuations, and anything that damps fluctuations must also generate fluctuations. However, while this theorem is powerful and widely known, it is not always clear how a fluctuation–dissipation relation (FDR) is linked to the underlying governing equations, such as those in the form of Eq. (1). Such a FDR resides in the integral forcing $G_{\tau,i}$ as given in Eq.(4), also referred to as the integral fluctuation–dissipation relation (IFDR).

Central to the IFDR is the total dissipation measured by d_τ. Being emerging only through time integration, this dissipation does not exist as a time rate of change and can hence not be part of the differential equations in the form of Eq. (1). A system in dynamical equilibrium has hence to be described by two principles that are complementary but not reducible to each other (J.-S. von Storch, 2026): one of them is formulated in the differential forcing F and takes the form of Eq. (1), and the other is expressed by the integral forcing $G_{\tau,i}$ and takes the form of Eq. (4). The former determines the individual trajectories, whereas the latter determines the statistics, such as variance and spectrum. For a system in dynamical equilibrium, these statistics are well defined and controlled by the constant external forcing.

1.3 THE AR(1) FRAMEWORK

To ease the applicability of the IFDR in practice, we consider the exact IFDR, but associated with only one integration time interval. While the full IFDR consists of G_τ in Eq. (4) for all values of $\tau > 0$, we consider a single value of τ, say $\tau = 1$ month. By letting $\alpha = d_1 + 1 = \rho_1$ and $n_{i+1} = f_{1,i}$, we obtain from Eqs. (3) and (4),

$$x_{i+1} = \alpha x_i + n_{i+1} \tag{7}$$

With $d_1 \in (-2, 0)$, the magnitude of α is smaller than 1. Equation (7) represents a stationary process, which has the same form as a first-order autoregressive (AR(1)) process. α describes the memory of this process, and n acts as the process's driving forcing, albeit n results from integrating the deterministic function F in Eq. (1) and is hence not stochastic and also not necessarily white. The variance of this process is given by

$$\sigma^2 = \frac{\sigma_n^2}{1-\alpha^2}, \tag{8}$$

where σ_n^2 is the variance of n.

While Eq. (7) is *exact* for describing the change of x over a one-month interval, it becomes *approximate* when applied to changes over intervals of length τ with $\tau \neq 1$ month. In the former case, the relevant statistics include the variance derived from monthly values of x, σ^2; the one-month memory characterized by α; and the variance of monthly fluctuating forcing σ_n^2. In the latter case, we have the same statistics, but for time intervals $\tau \neq 1$ month. While the variance remains unchanged, regardless of whether it is calculated from monthly values of x or from values sampled every τ time steps (provided the time series is stationary and sufficiently long), the parameters α and σ_n^2 associated with $\tau \neq 1$ month generally cannot be derived straightforwardly from their counterparts for $\tau = 1$ month. This is because the total dissipation of x within an interval of length τ results from the damping of interactions occurring during that interval, which can only be captured fully by integrating the whole set of equations in the form of Eq. (1), not by integrating Eq. (7). Consequently, d_τ and, with that, ρ_τ are generally not related to ρ_1 in the way predicted by Eq. (7). The spectrum obtained from Eq. (7)

$$S(f)=\frac{\sigma_n^2}{1+\alpha^2-2\alpha\cos(2\pi f)} \quad (9)$$

generally deviates from that given in Eq. (6).

Despite this discrepancy regarding lagged correlations, Eq. (7) captures the essence of the variance generation mechanics underlying both Hasselmann's stochastic climate models and the IFDR. In this paper, we will use Eq. (7) as an AR(1)-process for describing the intensity of oceanic internal variability, measured by the variance of x. Being exactly captured by Eq. (7), we can quantify the roles of memory and fluctuating forcing for this variance in terms of the two parameters in this AR(1)-process: α and σ_n^2. Moreover, we can quantify how these roles change with increasing grid resolution, as increasingly more fluctuations are resolved. We will do so both at the grid-point level and with respect to spatial scales.

1.4 PAPER OUTLINE

Section 2 describes the strategy for identifying ocean internal variability, the model configurations including post-processing procedures, the estimation of α and σ_n^2, and the technique used for spatial scale separation. In Subsection 3.1, we show that the AR(1)-framework does a good job in capturing the total variance of internal variability. We then identify in Subsection 3.2 a general relation between α and σ_n^2, which exists independent of grid resolution. The effect of grid resolution is studied by first considering the resolution-induced changes in the variance of internal variability, both with respect to the total variance and to the variances across spatial and temporal scales (Subsection 3.3), followed by a quantification of the resolution-induced changes in the two factors captured by an AR(1)-process—the strength of the fluctuating forcing and the memory—and their consequences for the total variance (Subsection 3.4). In Section 4, we draw the main conclusion of the paper.

2. METHOD

2.1 SEPARATING THE OCEAN INTERNAL VARIABILITY FROM TOTAL VARIABILITY

Ocean variability can be generated both internally and externally, the latter via time-varying surface fluxes arising from atmospheric variability. A widely used approach to isolate the ocean internal variability from the total variability employs an ensemble of identically forced ocean simulations, each initiated with minor perturbations, as conducted by Chervin, Gates, and Schneider (1974), Tang et al. (2019), or Lin, H. von Storch, and Chen (2023). The significance of internal variability for identifying deterministic signals in climate modeling has been stressed by Jain et al. (2023). The ensemble mean is regarded as the variability that can be traced back to the external forcing. The deviation from the ensemble mean is treated as the internal variability. Besides the ensemble simulation method, a more efficient strategy for isolating ocean internal variability is to drive an ocean model using a climatological atmospheric forcing, where the only external forcing is a seasonal cycle that is repeated every year. In this case, each simulated year can be treated as an ensemble member.

The second approach is used in this study, where one-year repeating forcing is used (Röske, 2006). After the mean seasonal cycle is removed from the model output, the residuals contain only internally generated variability. It should be noted, however, that this approach relies on the internal variability generated by the ocean model (ICON-O), which may differ from the true variability of the real ocean, and thus represents a potential limitation of the present analysis. Additionally, the variance of the residuals may depend on the phase of the annual cycle (e.g., differing between winter and summer). In this study, however, we estimate the lag-1 autocorrelation and noise variance using the full time series after removing the mean seasonal cycle, thereby implicitly assuming that these statistics are independent of the seasonal phase. This simplification is adopted for methodological consistency and to obtain robust estimates based on the available sample size, but it may neglect potential seasonally varying characteristics of internal variability.

2.2 MODEL CONFIGURATIONS AND POST-PROCESSING PROCEDURES

We employ the ocean general circulation model ICON-O, based on primitive equations (Korn, 2018; Korn et al., 2022a, 2022b). We use ICON-O in similar configurations but at different model resolutions. The horizontal grid resolutions are about 20, 10, and 5 km. It incorporates a sea-ice model describing sea ice thermodynamics and dynamics. The latter is based on the finite element sea-ice dynamics from FESIM (Danilov et al., 2015). The model uses a vertical z*- -coordinate (Adcroft & Campin, 2004) and 72 vertical levels. The grid type of ICON-O is a triangular grid with C-grid staggering. Horizontal momentum dissipation is applied via a biharmonic operator with a Smagorinsky-type viscosity coefficient of $2.7\times10^{-2}\,A_E^{3/2}\,\mathrm{m^4/s}$, where A_E is the area associated with an edge of a triangle grid (Griffies & Hallberg, 2000; Korn et al., 2022a). Vertical mixing follows a TKE scheme (Gaspar, Grégoris, & Lefevre, 1990) with a minimum TKE of $1.0\times10^{-6}\,\mathrm{m^2/s^2}$.

For the 20-km run, the eddy-induced tracer transport is represented using the GM-Redi scheme with a constant isopycnal diffusivity of $400\,\mathrm{m^2/s}$ and slope limiting of 10^{-3}, following a variational discretization suitable for unstructured grids (Korn, 2018). For 10 and 5 km runs, the GM-Redi scheme is turned off, since the model resolution is able to resolve a substantial part of mesoscale eddies. More details about the specific model configurations can be found in Korn et al. (2022a, 2022b).

The model is repeatedly forced by daily wind stress and heat and freshwater flux derived from the same forcing fields (Röske, 2006) every year. Turbulent latent and sensible

heat fluxes are computed using bulk formulae following Marsland et al. (2003), which helps reduce climate drift. In addition to the freshwater flux, the surface salinity is relaxed to an annual mean of the PHC-3.0 climatology (Steele, Morley, & Ermold, 2001) with a piston velocity of 2 m/90 days = 2.572×10^{-7} m/s for 20 and 10 km simulations, and 2 m/90 days = 8.573×10^{-6} m/s. The model temperature and salinity initial conditions are derived from the January 2010 mean values of the ORAS5 climatology (Zuo et al., 2019). The spin-up period is 20 years, and the subsequent 65 years of model daily output are used for the analysis in this paper.

We postprocess the model output by first removing the mean daily annual cycle from the daily model output, detrending the resulting daily anomalies, and averaging the daily anomalies to obtain the monthly anomaly time series. The analysis below is based mainly on the 65-year monthly anomaly time series of zonal and meridional velocity. We focus on velocity, but consider also temperature and salinity. For analytical convenience, a limited domain, 30–70°N, 0–80°W, which covers the eddy-rich region of the Gulf Stream extension in the North Atlantic, is considered. The original ICON triangular grid is remapped to a uniform 0.25° rectangular grid (nearest-neighbour remapping). All outputs from 20, 10, and 5 km simulations are projected onto the same grid, resulting in 160 × 320 (51,200) grid points.

2.3 REPRESENTING INTERNAL VARIABILITY WITHIN THE AR(1) FRAMEWORK

As explained in Subsection 1.3, the total variance of a monthly time series simulated by ICON at a certain resolution should be accurately represented by the respective AR(1)-process (see the consideration above Eq. (9)). Thus, we can attribute this total variance to two factors: one characterizes the dissipation with strength d_1, or the memory $\alpha = 1 + d_1$, and the other the strength of the fluctuating forcing n_t, σ_n^2.

In practice, α is estimated as lag-one-month autocorrelation ρ_1. After α is dertermined, the driving forcing n_i is identified as $x_{i+1}-\alpha_{xi}$, with x_{i+1} and x_i being the variable (e.g., zonal velocity) at two consecutive time points simulated by ICON. The memory associated with x is quantified by α. The variance of the fluctuating forcing $n_i = x_{i+1}-\alpha_{xi}$ is denoted by σ_n^2. For the ICON outputs, the estimates of the lag-one-month autocorrelation converge approximately using data longer than 25 years, regardless of whether the simulation is performed at 20, 10, or 5 km grid resolution. Therefore, given the 65-year simulation length, the estimation uncertainty is expected to be limited. Nevertheless, we acknowledge that rigorously quantifying the severity of the estimation errors would require formal statistical measures, such as confidence intervals or significance tests, which are not explicitly evaluated in the present study. The same procedure is used both at the grid-point level when x_t represents a variable at a grid point, and in EOF-space (see below) when x_t represents the coefficient time series (PC) of an EOF pattern.

2.4 AN EOF-BASED SCALE-SEPARATION METHOD

We utilized an alternative orthogonal linear basis—the EOFs basis—to separate the fields of velocity into different spatial scales. It is important to note that EOF modes are orthogonal by construction, whereas physical modes are not necessarily orthogonal. This discrepancy presents a general difficulty when interpreting EOFs as physical modes (H. von Storch & Zwiers, 1999). Except for the leading EOF, which can be chosen unconstrained by the orthogonality requirement, all subsequent EOFs are required to be orthogonal to one another. Nevertheless, an EOF representation is useful because it provides a linear basis transformation without loss of information. More importantly, our earlier studies have shown that the EOF expansion can be used as an effective tool for decomposing a field into a complete set of patterns with progressively smaller spatial scales. Although this scale-separation property is not evident from the mathematical formulation of EOF analysis, it has been demonstrated in several oceanographic applications (Lin et al., 2022; Tang, H. von Storch, & Chen, 2020). In the present paper, EOFs are used exclusively for spatial scale separation, rather than for identifying physically meaningful modes. Consequently, issues such as 'significance' and 'multiplicity' of EOFs are not central to our analysis.

We estimate EOFs from a combined dataset consisting of monthly velocity anomalies from the three simulations at 20, 10, and 5 km grid resolution, each covering 65 years. In this way, the EOFs are computed only once from the merged dataset, yielding a common set of EOF patterns that is identical for all three resolutions. Each simulation is then projected onto this shared EOF basis, ensuring that a given EOF index corresponds to the same spatial pattern and spatial scale across resolutions.

To derive the spatial scale of the j-th EOF, we use a geostatistical method (Tang, von Storch, & Chen, 2020) and calculate the spatial autocorrelation $S_j(k)$ of this EOF, where k indicates the lag in grid points. The spatial scale of this EOF, L_j, is obtained by integrating $S_j(k)$ from $k = 0$ to k^*, at which $S_j(k)$ drops below a threshold, and multiplying the result by the grid spacing $\Delta = 0.25°$ (corresponding to roughly 28 km). In this study, the threshold is chosen to be 0.7. With this calculation, the spatial variability of a variable in a geographical region is decomposed into EOFs, each having a characteristic length scale of L_j. The temporal variability associated with the j-th EOF is described by the variance and the spectrum of the j-th PC. The spatial scales are large in low-indexed EOFs and small in high-indexed EOFs, as found in Lin et al. (2022) and Tang, H. von Storch, and Chen (2020).

To illustrate how spatial scales vary with EOF index, Figure 1 presents four modes (EOF1, EOF10, EOF100, and EOF1000) of the zonal velocity at 95 m depth. EOF1 exhibits a dipole-like structure across the Gulf Stream extension, which may be related to a meridional

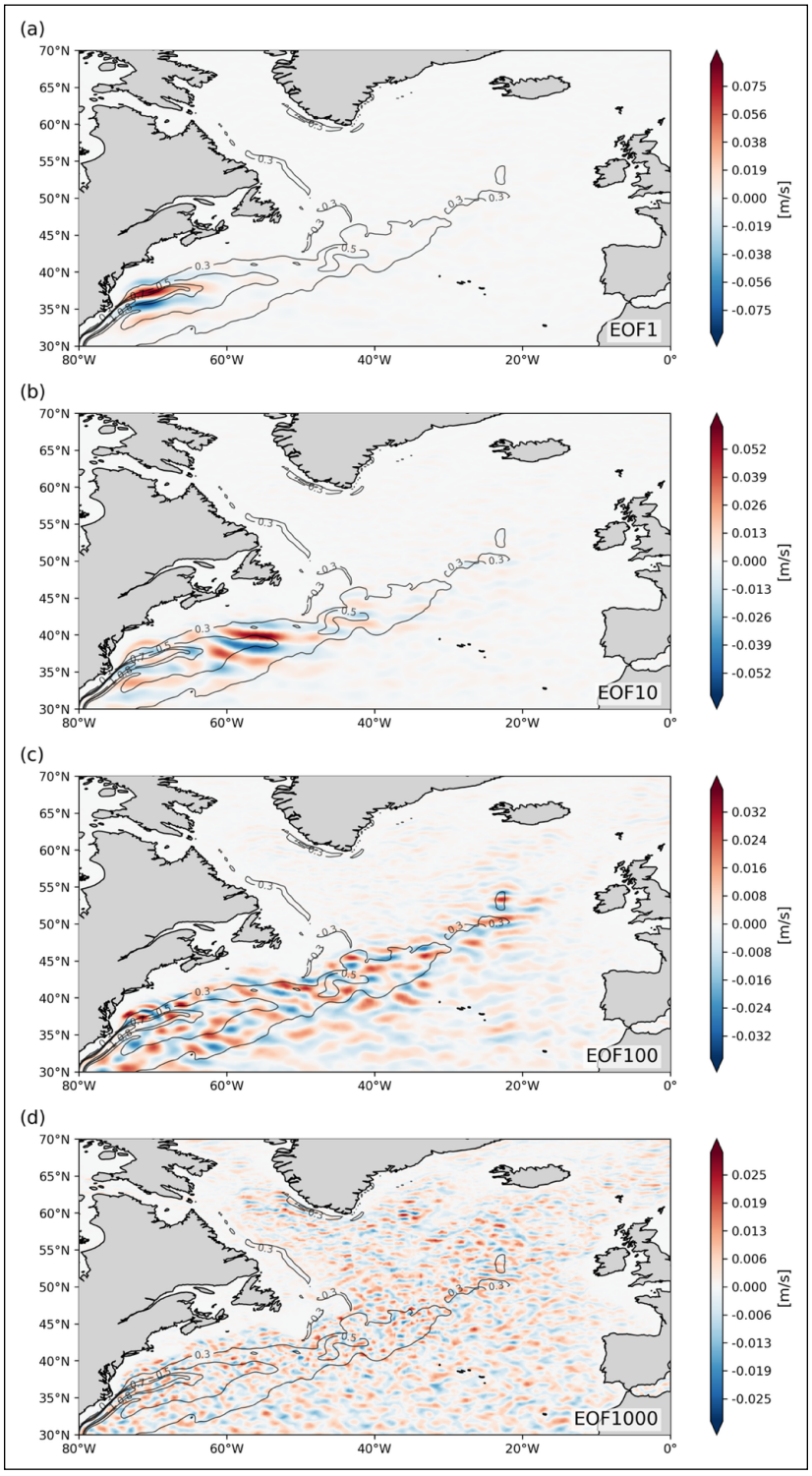


Figure 1 EOF1, EOF10, EOF100, and EOF1000, derived from zonal velocity at 95 m depth in all three simulations. Contours indicate the mean current speed in m/s.

displacement or meandering of the Gulf Stream path. EOF100 shows smaller-scale alternating positive and negative anomalies concentrated along the Gulf Stream and North Atlantic Current region, which may reflect mesoscale eddies. However, the alternating anomalies may also be deteriorated by the orthogonality constraint pointed out earlier and hence not represent the true structures of these eddies. Figure 2 quantifies the corresponding scale lengths for the first 1000 EOF modes. The results show a clear decrease in spatial scale with increasing EOF index, from approximately 82.5 km for the leading mode to about 30 km for higher-order modes. For the trailing EOFs, the estimated spatial scales become close to the grid spacing in the 20 km run (~28 km). This indicates that these EOF patterns have only weak spatial coherence and may be difficult to distinguish from spatial white noise, for which neighboring grid points are nearly statistically independent. Therefore, the physical interpretation of the trailing EOFs is limited, and EOFs are used in this paper solely for scale separation.

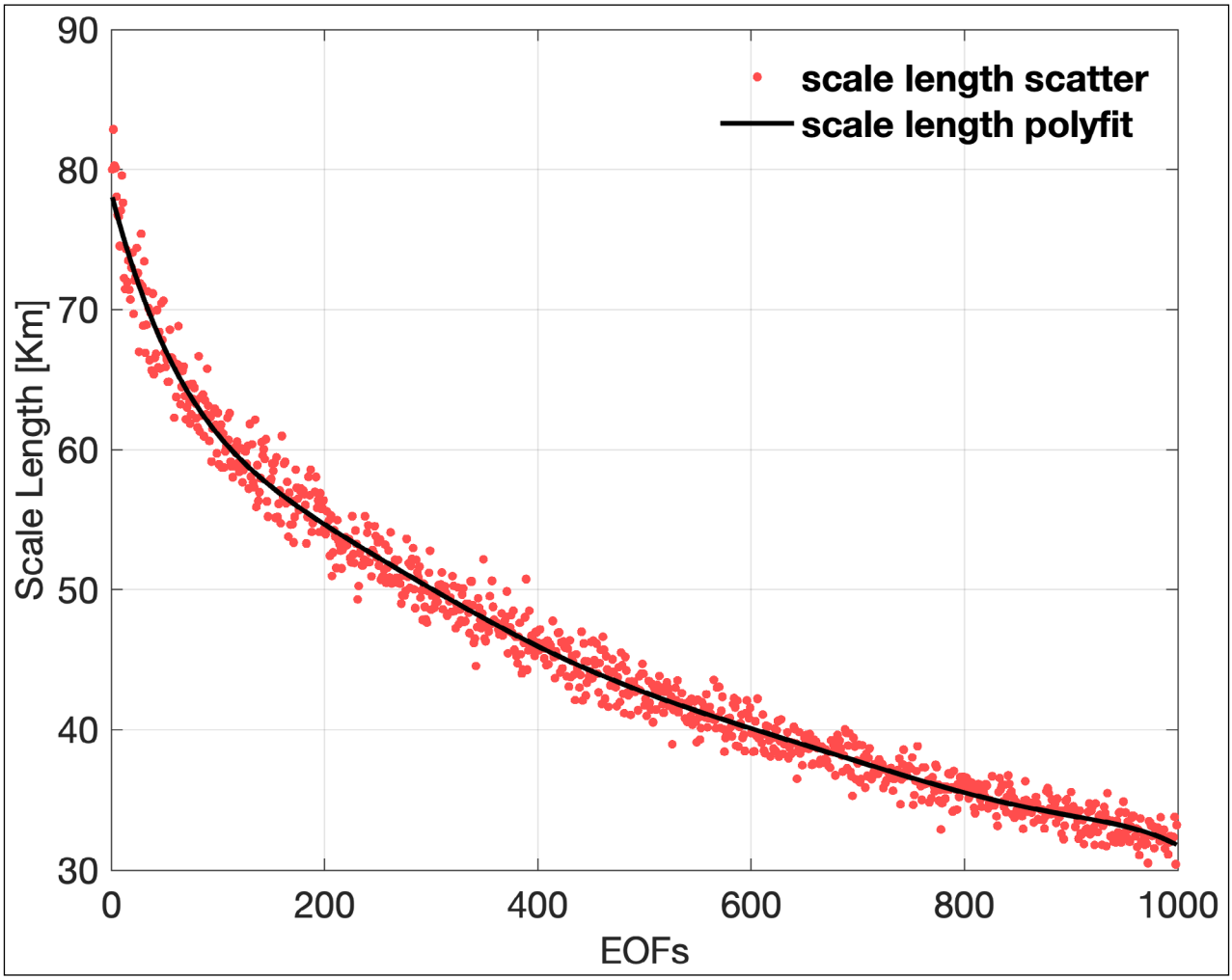


Figure 2 The estimated scale lengths (km) of the first 1000 EOFs derived from zonal velocity at 95 m depth in all three simulations. The red dots are the scales of each mode, and the black line is a smoothed interpolation using a third-order polynomial.

2.5 THE SPECTRAL SLOPE CALCULATION

For the sake of completeness, we also consider the spectral representation of internal variability. Since n is part of the integral of the deterministic function F, it is expected to deviate from white noise. To quantify this, we consider spectral slopes (SL), defined via the ordinary least-squares regression coefficient of $\log_{10}S_n(f)$ against $\log_{10}f$ over a prescribed fitting frequency band. Here, $S_n(f)$ denotes the power spectrum of n_t. Specifically, for a variable at each grid point (or for each PC), its *SL* was identified as the regression slope obtained by regressing $\log_{10}S_n(f)$ against $\log_{10}f$ for $f \in [f_{min}, f_{max}]$, where $f_{\min}$ and $f_{\max}$ are the lowest and the highest frequency resolved from a 65-year monthly time series.

3 RESULTS

3.1 INTERNAL VARIABILITY CAPTURED BY THE AR(1)-FRAMEWORK

In this subsection, we investigate to what extent the internal variability can be quantified in terms of the two parameters, α and σ_n^2, of the fitted AR(1)-process by comparing the variance predicted by Eq. (7) with the variance directly calculated from the model output. At the grid-point level, the AR(1)-variance shows a good spatial relationship with the internal variability intensity of zonal velocity (Figure 3a–c), temperature (Figure 4a–c), and salinity (Figure 5a–c) in simulations at all three grid resolutions. The result is not surprising, since the monthly variance σ^2 results from Eq. (3) with G_τ satisfying the IFDR given in Eq. (4) for τ equaling one month.

We next investigate how the variances associated with EOFs (Figure 1) are described by AR(1)-processes by considering spectra of the respective PCs. We present as examples spectra for PC1 and PC100 (gray lines in Figure 6), together with the spectra calculated according to Eq. (9) using σ_n^2 and α obtained by fitting AR(1) processes to monthly data (red lines). PC 100 is a randomly selected EOF index, and other PCs show a similar pattern. The spectra of zonal velocity PCs are, by and large, red, consistent with the redness associated with the AR(1)-spectrum. Red spectra are also found for other variables, for instance, meridional velocity, temperature, and salinity (not shown). Thus, internal variability on different spatial scales can, to a first-order approximation, be described by an AR(1) derived from monthly data.

Finally, we quantify the spectral characteristics of the fluctuating forcing n_t within the framework of an AR(1)-process, both at the grid-point level and in EOF-space. For this purpose, we calculate the spectral slopes of the spectra

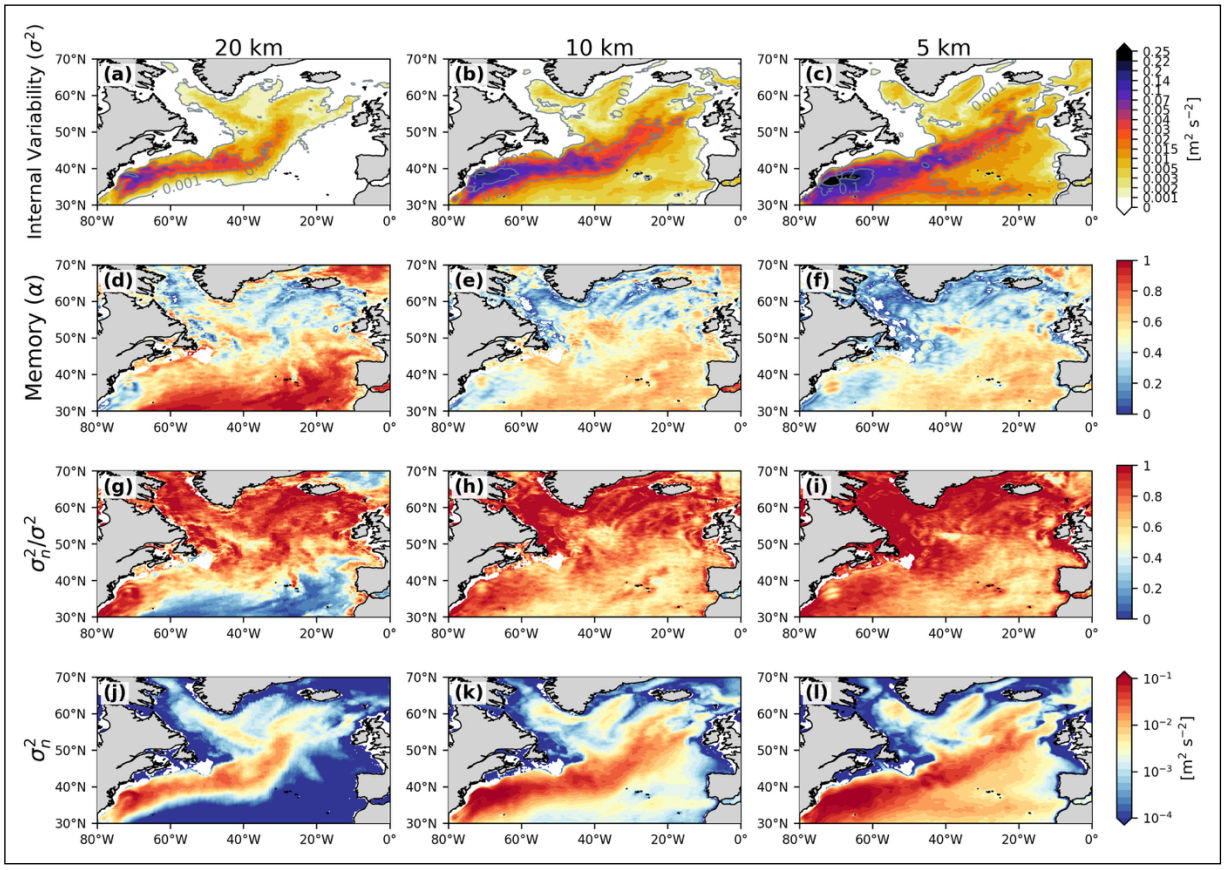


Figure 3 Spatial distribution of internal variability variance (first row), lag-one autocorrelation function (second row), normalized variance of the fluctuating forcing σ_n^2/σ^2 (third row), and fluctuating forcing σ_n^2 (fourth row) derived from **zonal velocity** at 95 m depth with a horizontal grid resolution of 20 km (left), 10 km (middle), and 5 km (right). **(a–c)** The color shading is internal variability simulated by ICON-O, and the contour lines are from the fitted AR(1)-process. **(d–f)** are on a logarithmic scale.

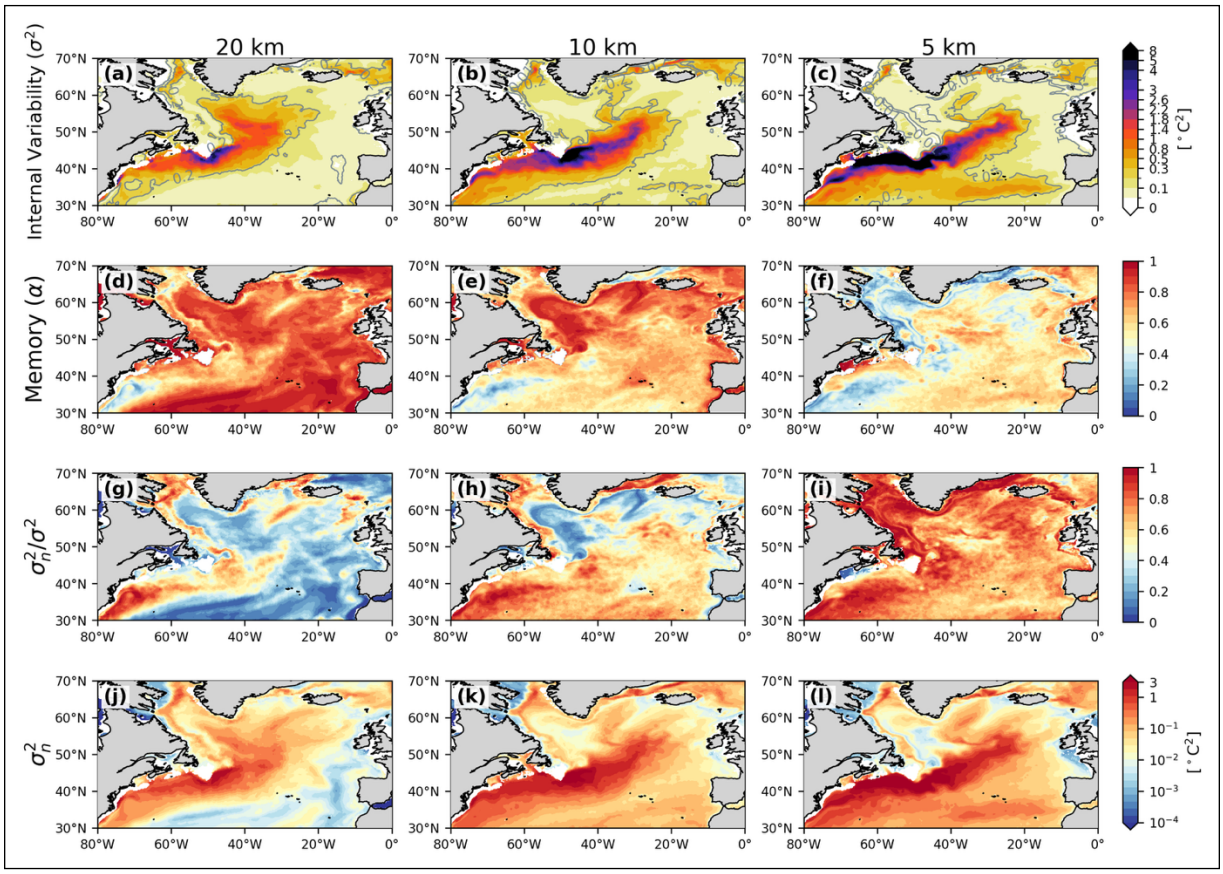


Figure 4 Same as Figure 3, but for temperature at 95 m depth.

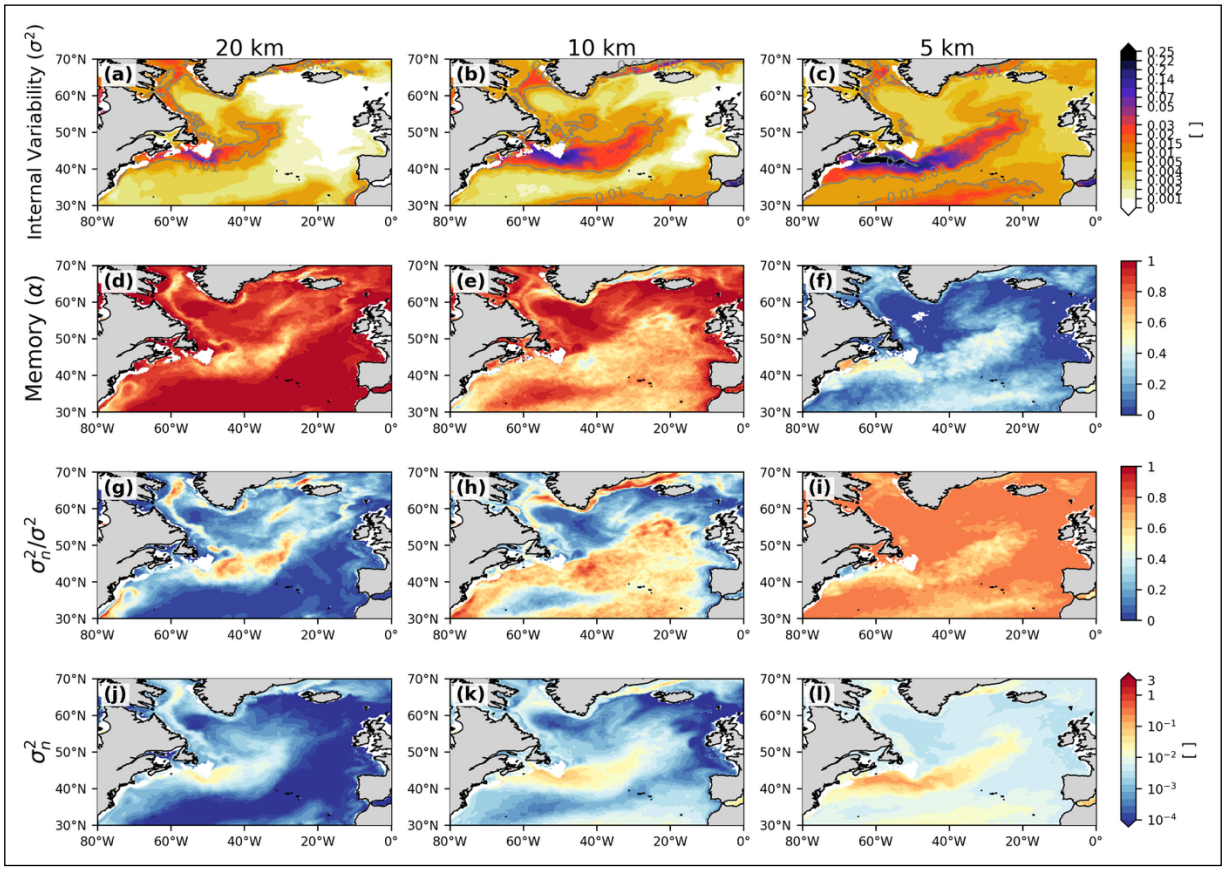


Figure 5 Same as Figure 3, but for salinity at 95 m depth.

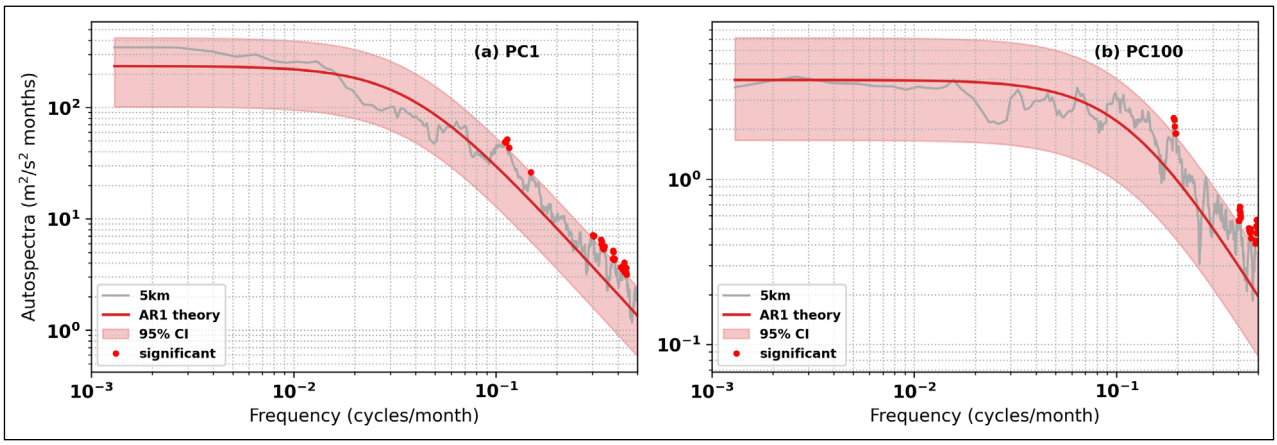


Figure 6 Spectra of the simulated internal variability (gray lines) and the fitted AR(1) process (red lines) for PC1 **(a)** and PC100 **(b)** obtained from the zonal velocity at 95 m in the 5 km simulation. The red shaded band represents the 95% confidence interval of the fitted AR(1) spectra. The multitaper method is applied for spectral smoothing, with a time–bandwidth product of 8 ($P = 8$), which effectively smooths over approximately 15 adjacent frequencies.

of n_t at each grid point (Figure 7a) and of n_t associated with PCs in EOF-space (Figure 7b) (see Section 2.5). In Figure 7a, the spectral slopes are close to zero but tend to be positive over most of the domain, except in some boundary regions. A negative spectral slope indicates higher variance at high frequencies than at low frequencies. We speculate that the negative spectral slopes near the boundaries may be partly attributable to stronger small-scale variability associated with sharp boundary currents and other local features. In Figure 7b, the slope tends to be slightly positive for many PCs. The tendency for having positive slopes suggests that the fluctuating forcing is slightly red.

To sum up, the results confirm that the fitted AR(1) model captures the total variance and describes the red spectral behavior to a considerable degree. The ability to capture the total variance justifies our subsequent interpretation of internal variability in terms of the two fitted AR(1) parameters, α and σ_n^2.

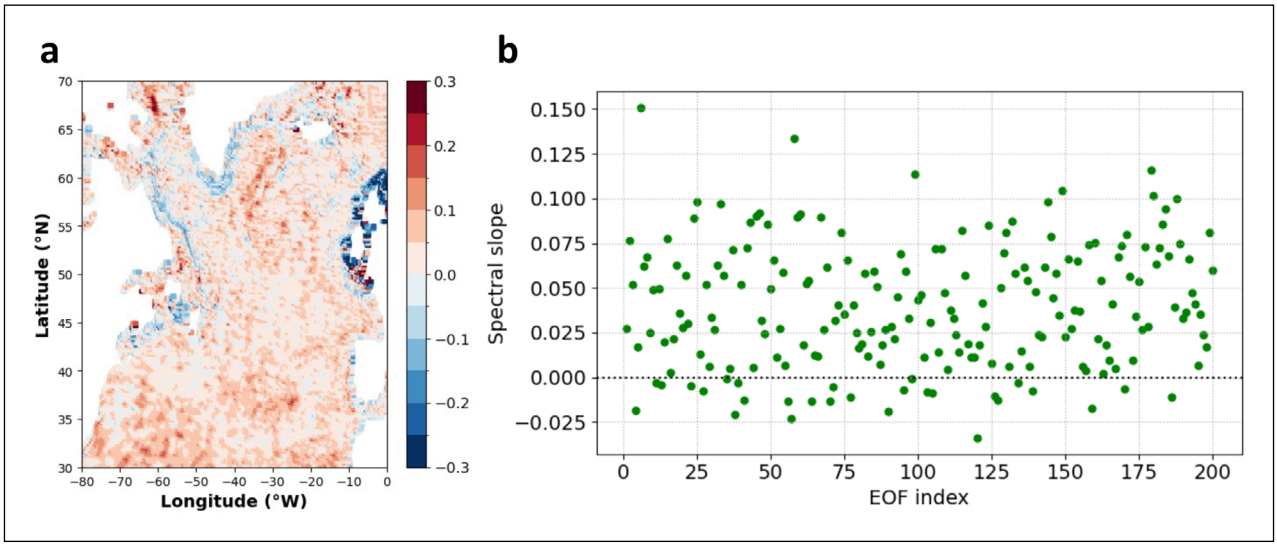


Figure 7 Spectral slopes of n_i at each grid point **(a)** and for the first 200 PCs **(b)** derived from zonal velocity at 95 m in the 5-km run.

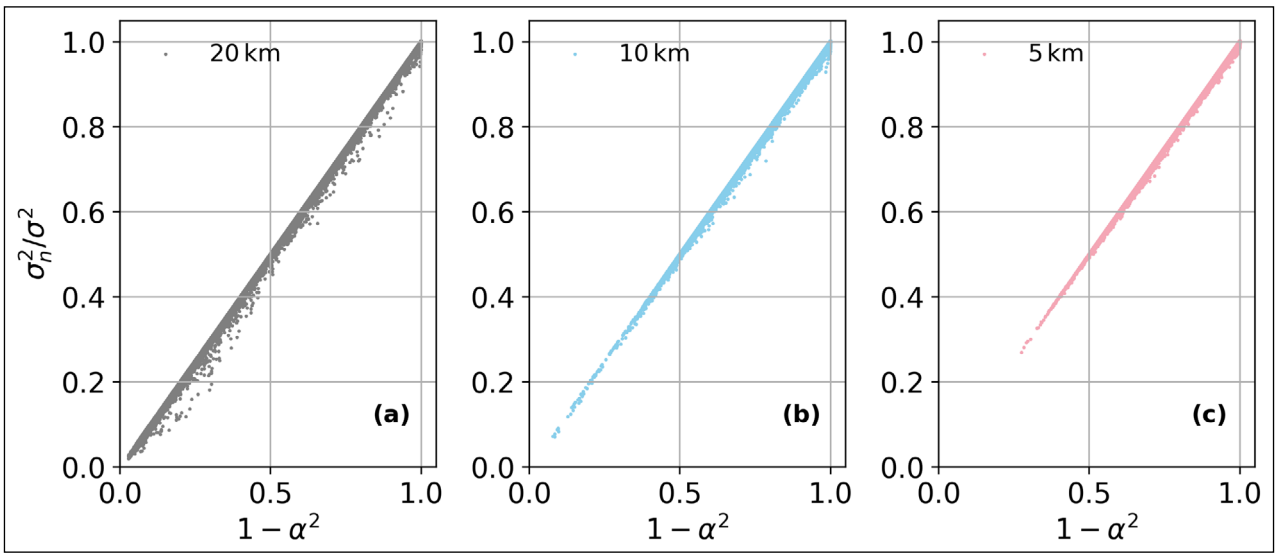


Figure 8 Relationship between $1-\alpha^2$ and the normalized variance of fluctuating forcing σ_n^2/σ^2, for zonal velocity at each grid point at 95 m (lag = 1 month).

3.2 RELATION BETWEEN α AND σ_n^2

As explained in Section 1, the joint effect of α and σ_n^2 determines the total variance, σ^2, thereby taking the form of Eq. (8). Consequently, α must be related to the variance of fluctuating forcing normalized by the variance of x (the variance of the considered variable), σ_n^2/σ^2, such that $(1-\alpha)^2 = \sigma_n^2/\sigma^2$. Consistent with this relation, the second and the third rows in Figures 3–5 show that the smaller α and hence the shorter the memory at one location, the stronger the fluctuating forcing per unit process variance σ_n^2/σ^2 at that location. When σ_n^2/σ^2 is plotted against $1-\alpha^2$ for each grid point (Figure 8), the values of σ_n^2/σ^2 against those of $1-\alpha^2$ lie essentially along the diagonal, which is expected given Eq. (8).

The spatial distributions shown in Figures 3–5 furthermore describe how internal variability arises from dissipation and fluctuations as two counteracting forcing mechanisms. Independent of the variable considered, the internal variability σ^2 (first rows in Figures 3–5) is strongest within the Gulf Stream and its extension, where the variance of the fluctuating forcing σ_n^2 is largest (last row in Figures 3–5), suggesting that the internal variability is generated by the fluctuating forcing n. Moreover, exactly at locations where σ_n^2 is largest, α (second rows in Figures 3–5) tends to have smaller values, suggesting that the stronger generation by the fluctuating forcing n is counteracted by a stronger dissipation. This is most apparent for temperature and salinity in the 20 km run (Figures 4d, j and 5d, j).

The spatial heterogeneity shown in Figures 3–5 reflects the dynamical conditions. In particular, the large variances in the Gulf stream and its extension region are likely the consequence of strong baroclinicity there. Away from the Gulf stream and its extension, more heterogeneous regional details are found. We also see that the inverse relation between σ_n^2 and α is not found in the subpolar region in Figure 3. To this end, we note that the inverse relation is an observation consistent with the more general FDR, that in order to obtain finite variance, the stronger the fluctuations,

the stronger the dissipation should be, or the shorter the memory (and hence the smaller α) should be. We note also that according to the IFDR, the relation refers to σ_n^2 and α associated with the integrated F in Eq. (1) (for velocity) at one grid point, not to those at different grid points. Thus, when σ_n^2 is larger at grid point A than at grid point B, α is not necessarily smaller at grid point A than at grid point B. Another aspect is that even at 5 km, the grid resolution may not be enough to fully resolve mesoscale eddies in the subpolar region. To what extent this impacts the distributions of σ_n^2 and α is not clear at this stage.

Figure 9 shows that the relationship between $1-\alpha^2$ and σ_n^2/σ^2, as given by Eq. (8), also holds for PCs. To simplify the description in EOF-space, in Figure 10, spatial scales shown in Figure 2 are aggregated into bins having a width of 5 km. σ^2, α, and σ_n^2 are first calculated for individual PCs and then averaged over those associated with EOFs, whose length scales fall within each of the considered bins. Figure 10 further shows that the scale dependence of the internal variability variance is largely consistent with that of fluctuating forcing: larger spatial scales are associated with larger σ_n^2 and larger σ^2, where both quantities decrease toward smaller scales. However, the memory α does not exhibit a consistent dependence on spatial scale. Thus, although the AR(1) relationship between memory and normalized fluctuating forcing remains valid after bin averaging, the out-of-phase relation—that is, the shorter the memory, the stronger the fluctuating forcing—is not clearly observed in the EOF space.

3.3 GRID RESOLUTION EFFECTS ON THE TOTAL VARIANCE AND THE SPECTRUM

At the grid-point level, increasing horizontal resolution markedly enhances internal variability at individual grid points (first rows of Figures 3–5). For 95 m zonal velocity (Figure 3a–c), the peak variance increases from 0.16 m^2/s^2 at 20 km to 0.27 m^2/s^2 at 10 km and 0.36 m^2/s^2 at 5 km (≈+135% overall). The domain-mean variance rises from 0.0052 to 0.0209 m^2/s^2 (≈+302% overall). The fraction of the domain with variance >0.1 m^2/s^2 expands from 0.1% at 20 km to 2.5% at 10 km and 3.9% at 5 km. Thus, increasing resolution not only intensifies local variance peaks but also enlarges the spatial extent of high-variance regions. Similar behavior is also found for temperature (Figure 4a–c) and salinity (Figure 5a–c). The increase in variance with increasing resolution reflects the model's ability to resolve an increasingly broad range of dynamical processes with increasing resolution, presumably those related to small-scale motions.

As more small-scale motions are resolved with increasing resolution from 20 km to 10 km and to 5 km, internal variability is enhanced at all time scales. The mean spectrum, obtained by averaging spectra of zonal velocity at all grid points within the analysis domain, is enhanced by roughly the same amount at all frequencies (Figure 11).

In the EOF-space, the internal variability at different spatial scales also increases with increasing resolution (Figure 10a). For each scale bin, the pink dot is above the blue dot, which in turn is above the gray dot. However, the increase is highly non-uniform: it is largest at the largest scale and becomes hardly noticeable for scales smaller than 50 km. Together with Figure 11, we conclude that the internal variability strengthens with increasing resolution nearly uniformly at all temporal scales, but most strongly at the largest spatial scale.

3.4 EFFECT OF GRID RESOLUTION ON α AND σ_n^2

Because α and σ_n^2 are generally related, a change in horizontal resolution that affects one of them is expected to affect the other as well. Moreover, the relation is expected to reflect the two counteracting mechanisms such that, if increasing horizontal resolution strengthens fluctuating forcing by resolving more small-scale processes, the memory should be shortened correspondingly.

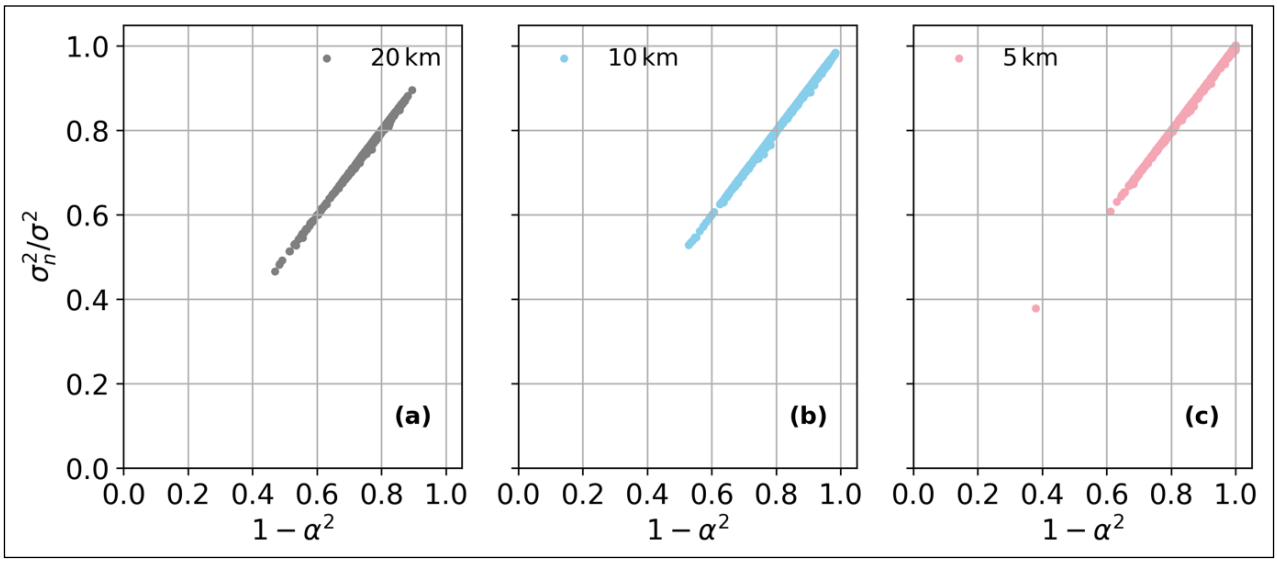


Figure 9 The relationship between $1-\alpha^2$ and the normalized variance of fluctuating forcing normalized by the variance of zonal velocity anomalies (95 m) for the first 1000 PCs (lag = 1 month).

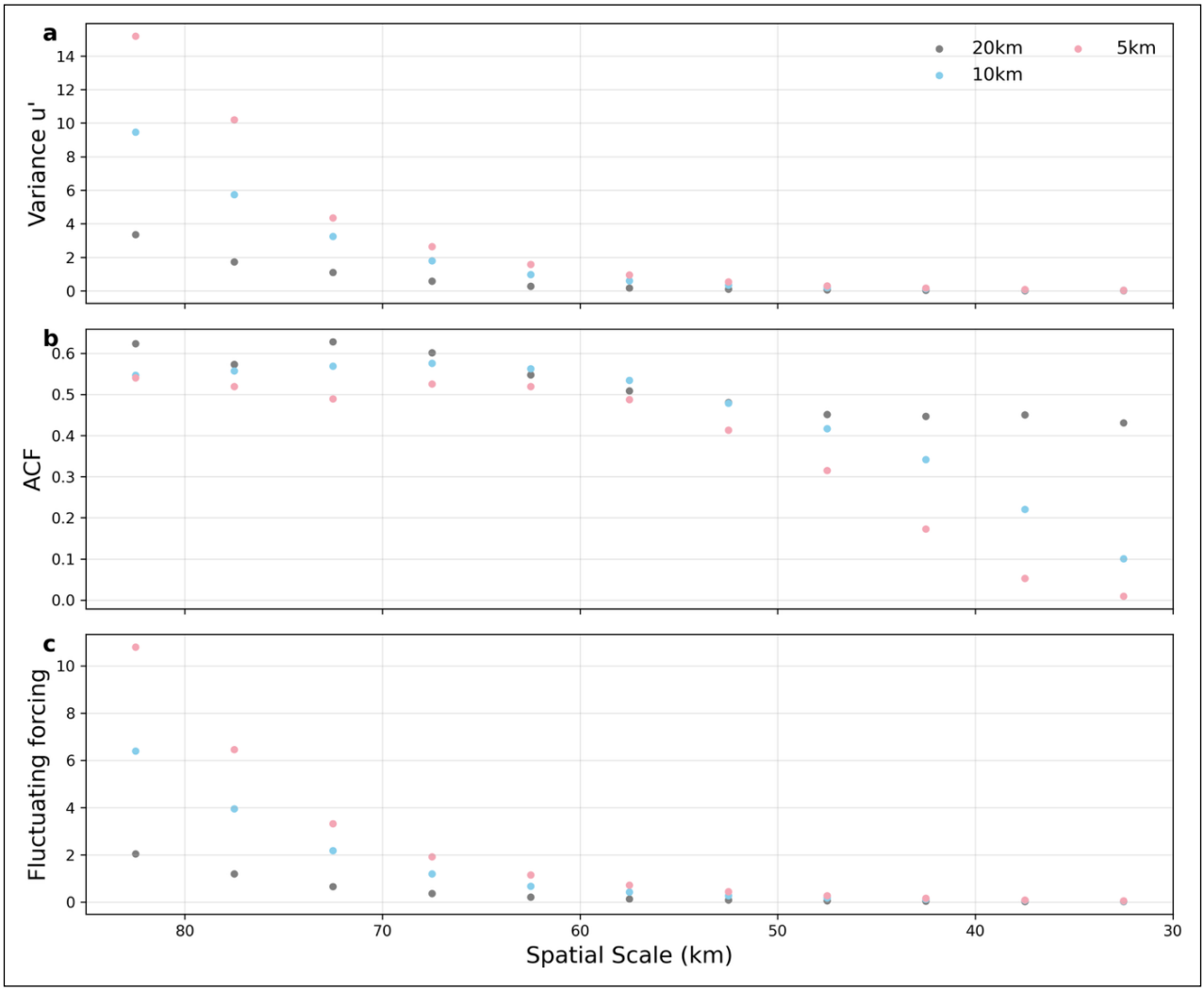


Figure 10 (a) Variance of the fitted AR(1)-process σ^2, **(b)** lag-one autocorrelation α, and **(c)** the variance of fluctuating forcing σ_n^2, as functions of spatial scale in the 20 km (gray), 10 km (light blue), and 5 km (pink) simulations. Each dot represents an average over the considered quantity (σ^2, or α, or σ_n^2) derived from PCs, whose spatial scales fall into a bin with bin size 5 km.

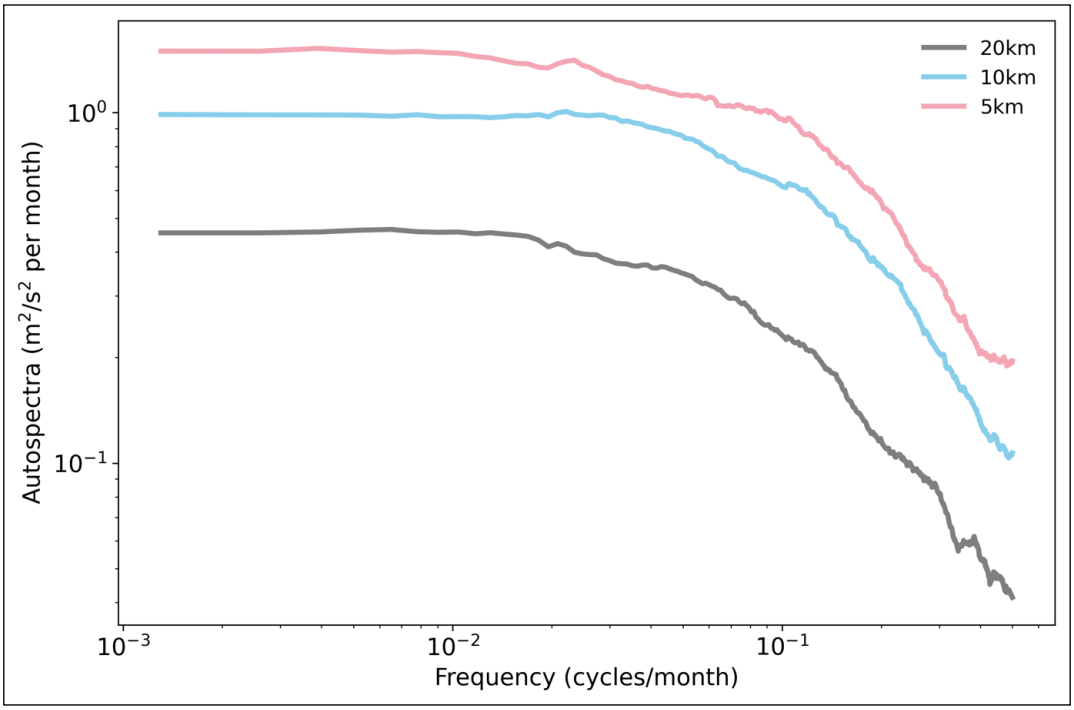


Figure 11 Domain-averaged local multi-taper estimates of the spectrum for zonal velocity at 95 m, derived from the simulations at 20 km (gray), 10 km (blue), and 5 km (pink) horizontal grid resolution. The time-bandwidth product of the multitaper method is 16 (P = 16).

This is indeed the case at the grid-point level: for zonal velocity (Figure 3j–l and d–f), the values of σ_n^2 increase, while the values of α decrease with increasing resolution. The decrease in α with increasing resolution is expected because higher resolution resolves more transient mesoscale and small-scale motions, enhancing high-frequency variability and accelerating decorrelation. This effect is particularly pronounced in the energetic Gulf Stream band (30–40°N), where passing mesoscale anomalies cause velocity at fixed grid points to decorrelate more rapidly.

The same tendency for α to decrease and σ_n^2 to increase with increasing resolution is also found for both temperature (Figure 4j–l and d–f) and salinity (Figure 5j–l and d–f). However, there are some detailed differences. At a grid resolution of 5 km, memory decreases more strongly for salinity than for either velocity or temperature, with α being close to zero over a large part of the domain. It is not clear whether and to what extent this result is related to the salinity restoring forcing used to complement the freshwater forcing at the sea surface.

In the EOF space, increasing horizontal resolution also leads to an increase in the variance of fluctuating forcing σ_n^2 across scales (Figure 10c). At all scales, σ_n^2 is the largest in the 5-km run, and smallest in the 20-km run. However, the increase of σ_n^2 with increasing resolution is largest at the largest scales. Increasing resolution also tends to reduce the memory α, especially for EOFs having scales smaller than 50 km (Figure 10b). At intermediate scales between 50 and 60 km, α derived from the 10-km run is the largest. At scales larger than 80 km, where the increase of σ_n^2 is the largest, the reduction in α due to increasing grid resolution from 10 to 5 km is hardly noticeable.

Generally, increasing grid resolution leads to a strengthening of fluctuating forcing and a reduction in memory. However, these resolution-induced changes vary strongly from grid point to grid point at grid-point level and from length scale to length scale in EOF space. In the plane spanned by $1–\alpha^2$ and σ_n^2/σ^2 these changes manifest as a systematic shift of the scatter toward larger values of both $1–\alpha^2$ and σ_n^2/σ^2 Figures 8 and 9). An exception concerns the first EOF in the 5-km run, which has a spatial scale of about 80 km and is depicted by the pink dot isolated from the scatter in Figure 9c. This EOF has, relative to all EOFs and all three grid resolutions, the longest memory α and the smallest normalized variance σ_n^2/σ^2.

According to Eq. (8), the resolution-induced effects on σ_n^2 and α generally compensate each other: increasing σ_n^2 leads to an increase in the variance of the AR(1)-process σ^2, whereas decreasing α, or equivalently an increase in $1–\alpha^2$, leads to a decrease in σ^2. However, the offset of this compensation is not zero. As shown by Figure 12, the resolution effect on σ_n^2 tends to outweigh the resolution effect on $1–\alpha^2$. In the

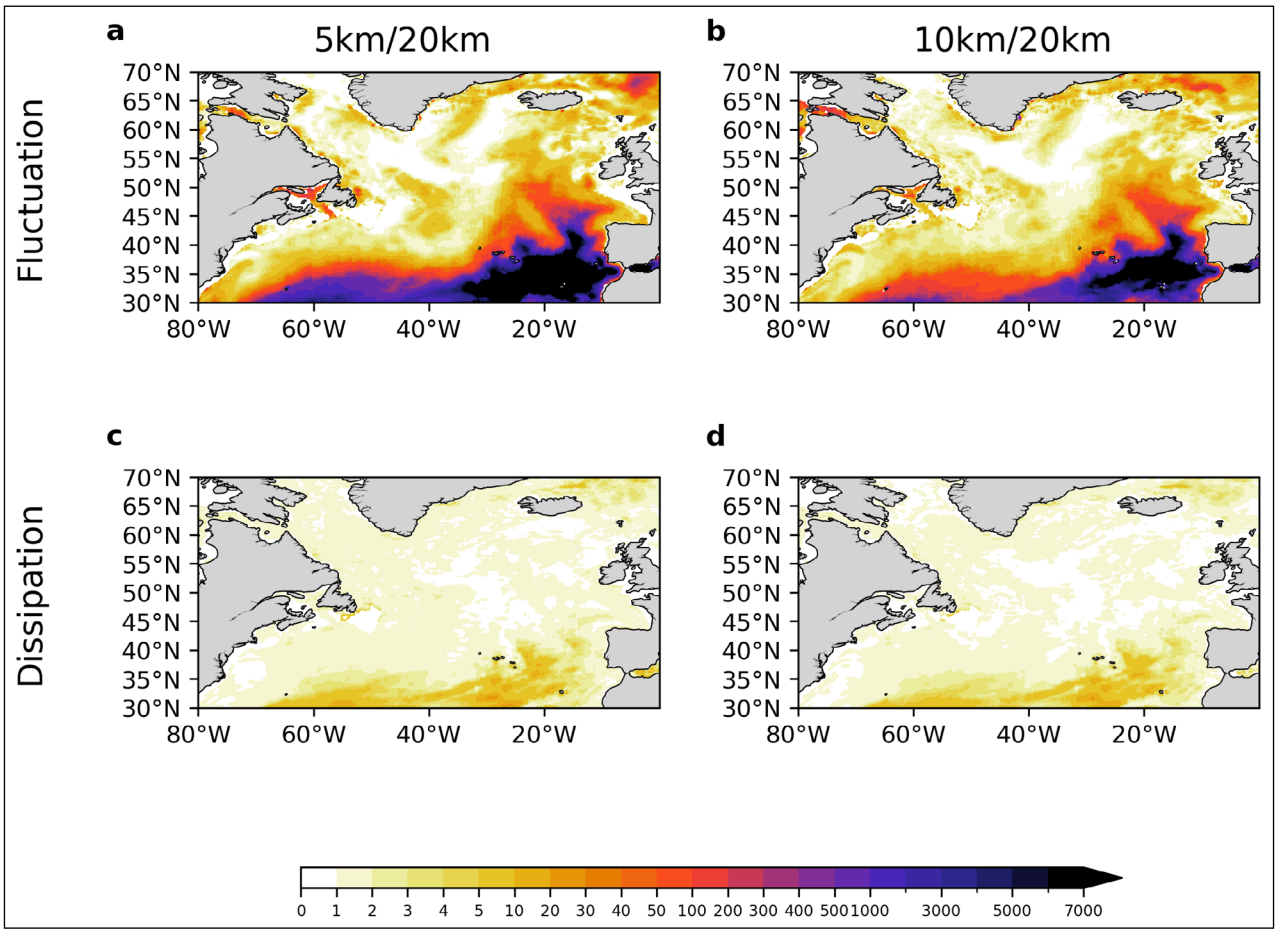


Figure 12 Ratios of σ_n^2 (top) and of $1-\alpha^2$ (bottom) in 5 km run to that in 20 km run **(a, c)**, and in 10 km run to that in 20 km run **(b, d)** for zonal velocity at 95 km.

southeast part of the considered domain, the value of σ_n^2 in the 5-km run is several orders of magnitude larger than that found in the 20-km run (Figure 12a), whereas the value of $1-\alpha^2$ is generally less than one order of magnitude larger in the 5-km run than in the 20-km run (Figure 12c). Similar ratios are found when resolution is increased from 20 to 10 km (Figure 12b and d). Due to the larger grid resolution effect on the strength of the fluctuating forcing than that on the memory, the total variance σ^2 increases with increasing resolution.

To sum up, increasing horizontal resolution strengthens the fluctuating forcing and generally reduces the memory, both at the grid-point level and in EOF space. Although stronger fluctuating forcing and shorter memory have opposing effects on the AR(1) variance, the resolution-induced increase in fluctuating forcing is generally larger. Consequently, the internal variability variance increases with increasing resolution.

4. CONCLUSION

In this paper, we analyze the grid resolution effect on the internal variability in the northern North Atlantic using the ICON-ocean model with three different horizontal resolutions (20, 10, and 5 km). The internal variability is described by an AR(1)-process, where the processes responsible for generating the internal variability are summarized into a dissipation term (reflected in memory) and a fluctuating forcing. We show that the variance of ocean internal variability can be well described by AR(1)-processes at the grid-point level and in EOF-space. We then quantify the resolution effects on the total variance σ^2 of internal variability in terms of the two factors embedded in an AR(1)-process: the memory characterized by lag-one correlation, α, and the strength of the fluctuating forcing described by the variance σ_n^2. The main findings are:

(1) Increasing grid resolution leads to a strengthening of internal variability across all temporal and spatial scales, with the strengthening being essentially uniform across the temporal scales, but highly non-uniform and strongest at the largest spatial scale.

(2) Independent of resolution, internal variability at different grid points is characterized by a general inverse relation between α and σ_n^2/σ^2, meaning that the stronger the fluctuating forcing, the shorter the memory (stronger the dissipation), reflecting the counteracting role of dissipation and fluctuations in generating internal variability. The exact magnitudes of α and σ_n^2 determine the total variance σ^2 such that $1-\alpha^2=\sigma_n^2/\sigma^2$ is always satisfied.

(3) Increasing resolution, which allows more small-scale variability to be resolved, leads to an amplification of the general relation between α and σ_n^2 per unit variance σ^2, characterized by a strengthening of fluctuating forcing and a decrease in ocean memory with increasing resolution.

(4) Increasing resolution has a stronger effect on fluctuating forcing than on memory, leading to a strengthening of the total variance of internal variability, despite a reduction in memory that tends to reduce the total variance.

The general relation between memory and fluctuating forcing is less pronounced in EOF-space, where a field variable is decomposed into EOFs having different spatial scales. While increasing grid resolution leads to a strengthening of fluctuating forcing at the largest scales, a clear decrease in memory is only found at the smallest scales. Further analysis is planned to explain this behavior.

We find that increasing grid resolution also leads to a reduction of oceanic memory, consistent with the resolution-induced reduction of atmospheric memory identified by Chen et al. (2025). Different from Chen et al. (2025), we show that the memory is closely linked to the fluctuating forcing that integrates all non-dissipative processes responsible for generating internal variability. Thus, increasing grid resolution not only allows a better representation of details of small-scale processes, but it also results in changes in statistics, such as the memory and variance.

The fluctuating forcing and memory diagnosed within our framework represent the integrated effects of the processes embodied in the underlying model equations. Thus, although the relatively large σ_n^2 in the Gulf Stream region is likely associated with instabilities arising from strong density gradients at particular times, we do not attempt to isolate the individual processes responsible for the variability at any given instant. Instead, we quantify their integrated effect, arising from all processes that have acted during the chosen integration period (one month in the present study). In other words, rather than examining each process individually, as in a conventional process-oriented analysis, we focus on the net effect of all interacting processes, thereby characterizing the statistical behavior of the system as a whole.

Ocean internal variability is a fundamental component of the climate system because it constitutes an intrinsic source of uncertainty in climate prediction/projection. At the same time, the dependence of its intensity on horizontal grid resolution is still not fully understood. This study provides a system-level perspective that advances the conceptual understanding of ocean internal variability and its sensitivity to model grid resolution. Our results are therefore of broad relevance to the climate and Earth system modeling community, particularly for the interpretation and the design of future high-resolution simulations, which have become a major frontier in Earth system modeling.

DECLARATION OF GENERATIVE AI AND AI-ASSISTED TECHNOLOGIES IN THE WRITING PROCESS

During the preparation of this work, the author used ChatGPT for improving language and readability.

DATA ACCESSIBILITY STATEMENT

The datasets generated during and/or analyzed during the current study are available from the corresponding author upon reasonable request.

ACKNOWLEDGEMENTS

Thanks to Fraser William Goldsworth for generating the 5-km simulation results; Helmuth Haak for helping with the numerical model setup.

FUNDING INFORMATION

This work is supported by the research funding of the Nobel Laureate (Klaus Hasselmann) Fellowship from Max Planck Society. This work used resources of the Deutsches Klimarechenzentrum (DKRZ) granted by its Scientific Steering Committee (WLA) under project bm1344 (EERIE resources).

COMPETING INTERESTS

The authors have no competing interests to declare.

AUTHOR AFFILIATIONS

Lin Lin orcid.org/0000-0002-8442-9722
Max Planck Institute for Meteorology, Hamburg, Germany

Jin-song von Storch orcid.org/0000-0002-2308-6834
Max Planck Institute for Meteorology, Hamburg, Germany; Center for Earth System Research and Sustainability (CEN), University of Hamburg, Hamburg, Germany

Hans von Storch orcid.org/0000-0002-5825-8069
Institute of Coastal Systems, Helmholtz Zentrum Hereon, Geesthacht, Germany

REFERENCES

Adcroft, A., & **Campin, J.-M.** (2004). Rescaled height coordinates for accurate representation of free-surface flows in ocean circulation models. *Ocean Modelling*, *7*(3–4), 269–284. https://doi.org/10.1016/j.ocemod.2003.09.003

Bador, M., Boé, J., Terray, L., Alexander, L. V., Baker, A., Bellucci, A., Haarsma, R., Koenigk, T., Moine, M., Lohmann, K., Putrasahan, D. A., Roberts, C., Roberts, M., Scoccimarro, E., Schiemann, R., Seddon, J., Senan, R., Valcke, S., & **Vanniere, B.** (2020). Impact of higher spatial atmospheric resolution on precipitation extremes over land in global climate models. *Journal of Geophysical Research: Atmospheres*, *125*(13), e2019JD032184. https://doi.org/10.1029/2019JD032184

Bilgen, S. I., & **Kirtman, B. P.** (2020). Impact of ocean model resolution on understanding the delayed warming of the Southern Ocean. *Environmental Research Letters*, *15*(11), 114012. https://doi.org/10.1088/1748-9326/abbc3e

Chen, T.-C., Goosse, H., Davrinche, C., Libera, S., Roberts, C., Aengenheyster, M., Strommen, K., Roberts, M., Ghosh, R., & **von Storch, J.-S.** (2025). Southern annular mode persistence and westerly jet: A reassessment using high-resolution global models. *Weather and Climate Dynamics*, *6*(4), 1179–1193. https://doi.org/10.5194/wcd-6-1179-2025

Chervin, R. M., Gates, W. L., & **Schneider, S. H.** (1974). The effect of time averaging on the noise level of climatological statistics generated by atmospheric general circulation models. *Journal of the Atmospheric Sciences*, *31*(8), 2216–2219. https://doi.org/10.1175/1520-0469(1974)031<2216:TEOTAO>2.0.CO;2

Danilov, S., Wang, Q., Timmermann, R., Iakovlev, N., Sidorenko, D., Kimmritz, M., Jung, T., & **Schröter, J.** (2015). Finite-element sea ice model (FESIM), version 2. *Geoscientific Model Development*, *8*(6), 1747–1761. https://doi.org/10.5194/gmd-8-1747-2015

Gaspar, P., Grégoris, Y., & **Lefevre, J.** (1990). A simple eddy kinetic energy model for simulations of the oceanic vertical mixing: Tests at station Papa and long-term upper ocean study site. *Journal of Geophysical Research: Oceans*, *95*(C9), 16179–16193. https://doi.org/10.1029/JC095iC09p16179

Grégorio, S., Penduff, T., Sérazin, G., Molines, J.-M., Barnier, B., & **Hirschi, J.** (2015). Intrinsic variability of the atlantic meridional overturning circulation at interannual-to-multidecadal time scales. *Journal of Physical Oceanography*, *45*(7), 1929–1946. https://doi.org/10.1175/JPO-D-14-0163.1

Griffies, S. M., & **Hallberg, R. W.** (2000). Biharmonic friction with a Smagorinsky-like viscosity for use in large-scale Eddy-permitting ocean models. *Monthly Weather Review*, *128*(8), 2935–2946. https://doi.org/10.1175/1520-0493(2000)128<2935:BFWASL>2.0.CO;2

Hasselmann, K. (1976). Stochastic climate models Part I. Theory. *Tellus*, *28*(6), 473–485. https://doi.org/10.1111/j.2153-3490.1976.tb00696.x

Hirschi, J. J.-M., Blaker, A. T., Sinha, B., Coward, A., de Cuevas, B., Alderson, S., & **Madec, G.** (2013). Chaotic variability of the meridional overturning circulation on subannual to interannual timescales. *Ocean Science*, *9*(5), 805–823. https://doi.org/10.5194/os-9-805-2013

Jain, S., Scaife, A. A., Shepherd, T. G., Deser, C., Dunstone, N., Schmidt, G. A., Trenberth, K. E., & **Turkington, T.** (2023). Importance of internal variability for climate model assessment. *Npj Climate and Atmospheric Science*, *6*(1). https://doi.org/10.1038/s41612-023-00389-0

Korn, P. (2018). A structure-preserving discretization of ocean parametrizations on unstructured grids. *Ocean Modelling*, *132*, 73–90. https://doi.org/10.1016/j.ocemod.2018.10.002

Korn, P., Brüggemann, N., Jungclaus, J. H., Lorenz, S. J., Gutjahr, O., Haak, H., Linardakis, L., Mehlmann, C., Mikolajewicz, U., Notz, D., Putrasahan, D. A., Singh, V., von Storch, J.-S., Zhu, X., & **Marotzke, J.** (2022a). ICON-O: The ocean component of the ICON Earth System Model: Global simulation characteristics and local telescoping capability. *Journal of Advances in Modeling Earth Systems*, *14*(10), e2021MS002952. https://doi.org/10.1029/2021MS002952

Korn, P., Brüggemann, N., Jungclaus, J. H., Lorenz, S. J., Gutjahr, O., Haak, H., Linardakis, L., Mehlmann, C., Mikolajewicz, U., Notz, D., Putrasahan, D. A., Singh, V., von Storch, J. -S., Zhu, X., & **Marotzke, J.** (2022b). ICON-O: The ocean component of the ICON Earth System Model: Global simulation characteristics and local telescoping capability. *Journal of Advances in Modeling Earth Systems*, *14*(10), e2021MS002952. https://doi.org/10.1029/2021MS002952

Lin, L., von Storch, H., & **Chen, X.** (2023). The Stochastic Climate Model helps reveal the role of memory in internal variability in the Bohai and Yellow Sea. *Communications Earth & Environment*, *4*(1), 347. https://doi.org/10.1038/s43247-023-01018-7

Lin, L., von Storch, H., Guo, D., Tang, S., Zheng, P., & **Chen, X.** (2022). The effect of tides on internal variability in the Bohai and Yellow Sea. *Dynamics of Atmospheres and Oceans*, *98*, 101301. https://doi.org/10.1016/j.dynatmoce.2022.101301

Marsland, S. J., Haak, H., Jungclaus, J. H., Latif, M., & **Röske, F.** (2003). The Max-Planck-Institute global ocean/sea ice model with orthogonal curvilinear coordinates. *Ocean Modelling*, *5*(2), 91–127. https://doi.org/10.1016/S1463-5003(02)00015-X

Penduff, T., Juza, M., Barnier, B., Zika, J., Dewar, W. K., Treguier, A.-M., Molines, J.-M., & **Audiffren, N.** (2011). Sea level expression of intrinsic and forced ocean variabilities at interannual time scales. *Journal of Climate*, *24*(21), 5652–5670. https://doi.org/10.1175/JCLI-D-11-00077.1

Roberts, M. J., Camp, J., Seddon, J., Vidale, P. L., Hodges, K., Vanniere, B., Mecking, J., Haarsma, R., Bellucci, A., Scoccimarro, E., Caron, L.-P., Chauvin, F., Terray, L., Valcke, S., Moine, M.-P., Putrasahan, D., Roberts, C., Senan, R., Zarzycki, C., & **Ullrich, P.** (2020). Impact of model resolution on tropical cyclone simulation using the HighResMIP–PRIMAVERA multimodel ensemble. *Journal of Climate*, *33*(7), 2557–2583. https://doi.org/10.1175/JCLI-D-19-0639.1

Röske, F. (2006). A global heat and freshwater forcing dataset for ocean models. *Ocean Modelling*, *11*(3–4), 235–297. https://doi.org/10.1016/j.ocemod.2004.12.005

Steele, M., Morley, R., & **Ermold, W.** (2001). PHC: A global ocean hydrography with a high-quality Arctic Ocean. *Journal of Climate*, *14*(9), 2079–2087. https://doi.org/10.1175/1520-0442(2001)014<2079:PAGOHW>2.0.CO;2

Tang, S., von Storch, H., & **Chen, X.** (2020). Atmospherically forced regional ocean simulations of the South China Sea: Scale dependency of the signal-to-noise ratio. *Journal of Physical Oceanography*, *50*(1), 133–144. https://doi.org/10.1175/JPO-D-19-0144.1

Tang, S., von Storch, H., Chen, X., & **Zhang, M.** (2019). "Noise" in climatologically driven ocean models with different grid resolution. *Oceanologia*, *61*(3), 300–307. https://doi.org/10.1016/j.oceano.2019.01.001

von Storch, H., & **Zwiers, F. W.** (1999). *Statistical analysis in climate research*. Cambridge University Press. https://doi.org/10.1017/CBO9780511612336

von Storch, J.-S. (2022). On equilibrium fluctuations. *Tellus A: Dynamic Meteorology and Oceanography*, *74*(2022), 364–381. https://doi.org/10.16993/tellusa.25

von Storch, J.-S. (2024). Randomness and integral forcing. *Tellus A: Dynamic Meteorology and Oceanography*, *76*(1), 74–89. https://doi.org/10.16993/tellusa.4065

von Storch, J.-S. (2026). Principles of equilibrium fluctuations. *Physica A: Statistical Mechanics and Its Applications*, *683*, 131218. https://doi.org/10.1016/j.physa.2025.131218

Wang, Q., Shu, Q., Bozec, A., Chassignet, E. P., Fogli, P. G., Fox-Kemper, B., Hogg, A. McC., Iovino, D., Kiss, A. E., Koldunov, N., Le Sommer, J., Li, Y., Lin, P., Liu, H., Polyakov, I., Scholz, P., Sidorenko, D., Wang, S., & **Xu, X.** (2024). Impact of increased resolution on Arctic Ocean simulations in Ocean Model Intercomparison Project phase 2 (OMIP-2). *Geoscientific Model Development*, *17*(1), 347–379. https://doi.org/10.5194/gmd-17-347-2024

Wang, X., Yu, Y., Yu, Z., & **Lin, P.** (2025). Impact of refined oceanic model resolution on the simulation of Atlantic meridional overturning circulation in LICOM3. *Atmospheric and Oceanic Science Letters*, 100615. https://doi.org/10.1016/j.aosl.2025.100615

Zuo, H., Balmaseda, M. A., Tietsche, S., Mogensen, K., & **Mayer, M.** (2019). The ECMWF operational ensemble reanalysis–analysis system for ocean and sea ice: A description of the system and assessment. *Ocean Science*, *15*(3), 779–808. https://doi.org/10.5194/os-15-779-2019

TO CITE THIS ARTICLE:
Lin, L., von Storch, J.-S., & von Storch, H. (2026). Impacts of Model Resolution on Ocean Internal Variability in the Northern North Atlantic Analyzed within the Framework of AR(1)-Process. *Tellus*, *79*(1), 232–248. https://doi.org/10.16993/tellus.4138

Submitted: 06 January 2026 **Accepted:** 05 October 2026 **Published:** 13 November 2026

COPYRIGHT:
© 2026 The Author(s). This is an open-access article distributed under the terms of the Creative Commons Attribution 4.0 International License (CC-BY 4.0), which permits unrestricted use, distribution, and reproduction in any medium, provided the original author and source are credited. See https://creativecommons.org/licenses/by/4.0/.

Tellus is a peer-reviewed open access journal published by Stockholm University Press.